VI International Conference on Particle-based Methods – Fundamentals and Applications
PARTICLES 2019
E. Oñate, M. Bischoff, D.R.J. Owen P. Wriggers, , & T. Zohdi (Eds)

EFFECT OF PARTICLE DIAMETER ON AGGLOMERATION DYNAMICS IN MULTIPHASE TURBULENT CHANNEL FLOWS

L.F. MORTIMER AND M. FAIRWEATHER

University of Leeds
School of Chemical and Process Engineering, University of Leeds, Leeds, LS2 9JT, UK
l.f.mortimer@leeds.ac.uk

Key words: Direct numerical simulation, Lagrangian particle tracking, Particle-laden flow, Fluid dynamics, Agglomeration, Four-way coupling, Channel flow

Abstract. The present work uses a fully coupled direct numerical simulation-Lagrangian particle tracking solver in conjunction with an interaction energy-based deterministic agglomeration algorithm to determine the effect of particle diameter on the aggregation properties of a wall-bounded, particle-laden channel flow at shear Reynolds number, $Re_\tau = 180$. Three primary particle diameters are considered of relevance to the nuclear industry resembling 200μm - 400μm calcite particles dispersed in water, with a Hamaker constant of 3.8×10^{-20} J. The simulations are initialized with randomly dispersed particles of numbers calculated to ensure a constant volume fraction $\Phi_P = 10^{-3}$. Analysis is focused on elucidating the collision and agglomeration behaviour throughout the channel flow over time. A statistically steady state for collision and agglomeration rate is observed 10 non-dimensional time units after the particles have been injected which persists until at least $t^* = 50$. Results indicate a decrease in particle agglomeration efficiency as diameter is increased, which provides for a reduction in agglomeration rate at large time scales as the particles begin to aggregate and the mean agglomerate diameter increases. Further to this, the normalized number of collisions is similar in all simulations, with the smallest particles showing a slightly increased collision rate. Arguments associated with energy dispersed in collisions are presented to substantiate these findings. Collision rates across the channel are approximately constant with an increase close to the walls which, when normalized by the total number of primary particles, are actually favoured by smaller particles. Finally, agglomeration outcomes after a collision are shown to be more likely towards the channel centreline, since the particle dynamics in this region favour collisions with low relative velocity.

1 INTRODUCTION

Particle-laden flows with high mass loading are ubiquitous in nature and industry, such as atmospheric transport [1], blood drop forensics [2] and mineral processing [3]. Of relevance to this study is the nuclear industry, which depends on a comprehensive understanding of the particle-scale and system-scale processes associated with such flows in order to predict the long-term behaviour of waste suspension slurries [4]. At present, a key challenge exists in the ability to transport legacy nuclear waste material from historic ponds and silos at Sellafield, UK to interim locations where they can be safely stored. In order to do so, knowledge must be generated surrounding the aggregation and interaction dynamics of densely dispersed two-

phase fluid-solid flow systems. Of importance is the long term morphology of the particles (size, shape and interaction profile information) in order to predict potential hazards over long time-frames. Fundamental knowledge of this kind could also be used to improve current waste transport designs.

At high particle-fluid volume fractions, the dynamics of both phases are governed by interparticle collisions, which in most cases can lead to particle-particle adhesion or agglomeration due to electrokinetic interactions between the dispersed phase elements [5]. These mechanisms cause long-term particle morphology changes which increase the risk of blockages, local concentration peaks and poor heat-transfer conditions. Furthermore, modifications to the particle concentration field can then impact on the turbulence properties of the carrier fluid, affecting the transport efficiency. The present study focuses on developing computational tools to predict and quantify these phenomena, before exploiting them to elucidate the physics surrounding long-term particle-particle agglomeration in wall-bounded flows.

Motivated by the inherent impracticality of experimental studies to capture individual particle-particle interactions on a sufficient analytical scale, along with the recent advances in computational performance, fluid dynamics modelling has become a powerful tool to study such phenomenon for multi-phase fluid flows. Typically, the carrier phase is simulated using direct numerical simulation (DNS) or large eddy simulation (LES), however the latter has been shown to provide less accurate results for dense flows, since the unresolved scales fail to provide the correct two-way coupled forcing field back to the continuous phase [6], despite its computational cost advantages. Over the last few decades, DNS has been used along with Lagrangian particle tracking (LPT) to study a wide variety of turbulent systems containing particles, droplets and bubbles. The majority of these studies simulate particles in isotropic or wall-bounded turbulence and focus on behaviours such as dispersion, wall deposition, entrainment, resuspension, turbulence modulation and particle-particle collisions.

The focus of the present work relies on modelling post-collision effects (i.e. adhesion or bouncing). Work in this field is sparse, despite most real multiphase systems possessing electrokinetic dynamics at close interparticle distances [7]. Typical attempts to consider agglomeration are divided into either stochastic [8], wherein the particles stick based on the outcome of a random process, or deterministic [9] approaches. In the deterministic approach an adhesion requirement is usually based on collision momentum [10, 11], kinetic/potential energy considerations [12] or local flow properties.

The present work utilizes a model based on energy budget arguments during the collision which has previously been successfully applied to the LES of multiphase turbulent channel flows [13]. We here aim to expand on this work by switching to a DNS continuous phase solver, which will allow us to further elucidate the fundamental dynamics which determine particle-particle adhesion throughout the various regions of the turbulent channel flow. In order to relate the present work to the systems present in the nuclear waste processing industry, we consider mechanical and chemical properties matching those of spherical calcite particles in water [14], which is a frequently used simulant for radioactive waste material.

2 METHODOLOGY

2.1 Fluid flow simulation

The spectral element method-based code Nek5000 is used to obtain a carrier-fluid field representing a fully developed turbulent channel flow. This was chosen due to its impressive and reliable testing and validation history, along with its scalability in terms of parallelisation. The element discretization ensures that all the smallest length and time scales are resolved, down to the structures and processes associated with the Kolmogorov length scale. The code solves the incompressible Navier-Stokes (NS) equations to 7th order accuracy on a Cartesian structured grid which consists of 27 × 18 × 23 elements (i.e. 5.7M nodes). The elements are distributed more densely in the near-wall region in order to capture the smaller scales of turbulence in this location. The non-dimensional NS equations are presented in Eqs. (1) and (2), with distances, velocities and densities normalized by the channel half-height, δ, the bulk velocity, U_B, and the fluid phase density, ρ_F, respectively. From here on, any quantity with an asterisk (*) denotes a variable non-dimensionalised in this manner.

$$\boldsymbol{\nabla} \cdot \boldsymbol{u}^* = 0 \tag{1}$$

$$\frac{\partial \boldsymbol{u}^*}{\partial t^*} + \boldsymbol{u}^* \cdot \boldsymbol{\nabla} \boldsymbol{u}^* = -\boldsymbol{\nabla} p^* + \frac{1}{Re_B} \boldsymbol{\nabla} \cdot \boldsymbol{\tau}^* + \boldsymbol{f}^*_{2W,i} + \boldsymbol{f}^*_{PG} \tag{2}$$

Here, $\boldsymbol{u}^*$ is the fluid velocity, p^* is the fluid pressure, Re_B is the bulk Reynolds number defined as $Re_B = U_B \delta / \nu_F$, ν_F is the fluid kinematic viscosity and $\boldsymbol{\tau}^*$ is the viscous stress tensor. The additional term $\boldsymbol{f}^*_{2W,i}$ is cell-dependent and accounts for the two-way momentum exchange between particles in that cell and the surrounding fluid. Finally, the term $\boldsymbol{f}^*_{PG}$ is constant and accounts for a pressure gradient across the channel in the streamwise direction.

The NS equations are solved across the computational position domain (x, y, z), which corresponds to a $12\delta \times 2\delta \times 6\delta$ channel as illustrated in Fig. 1. We define x to be the streamwise direction, y to be the wall-normal direction, and z to be the spanwise direction. Periodic boundary conditions are enforced in the streamwise and spanwise directions, whereas the wall-normal axis uses no-slip conditions at $y^* = \pm\delta$. The flow rate is maintained by a constant pressure gradient. Using non-dimensional parameters this is:

$$\boldsymbol{f}^*_{PG} = \frac{\partial p^*}{\partial x^*} \hat{\boldsymbol{x}} = \left(\frac{Re_\tau}{Re_B} \right)^2 \hat{\boldsymbol{x}} \tag{3}$$

where Re_τ is the shear Reynolds number for the flow. The present simulations were carried out at $Re_B = 2800$ which corresponds to $Re_\tau = 180$. A constant fluid timestep of $\Delta t^*_F = 0.01$ was used throughout.

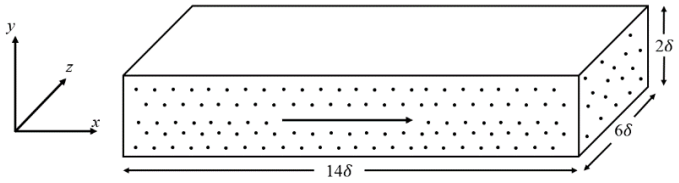

Figure 1: Schematic of the multi-phase turbulent channel flow at $Re_\tau = 180$.

2.2 Particle advection

To simulate the advection of large quantities of solid spherical particles throughout the fluid flow field, an LPT has been developed which runs concurrently after each fluid solution step. The non-dimensional Newtonian equations of motion for each particle are integrated to obtain trajectories at each timestep. The equation is based on the Maxey-Riley (MR) force-balance [15] and in the present work, contributions from drag forces, along with shear lift, virtual mass and pressure gradient forces are considered, since the study entails particles with low density ratio. The only term we neglect from the MR equation is the Basset history force term which would involve very long computation times for minimal increase in accuracy [16].

The Newtonian equations of motion for velocity and acceleration are, respectively:

$$\frac{\partial \boldsymbol{x}_P^*}{\partial t^*} = \boldsymbol{u}_P^* \tag{4}$$

$$\frac{\partial \boldsymbol{u}_P^*}{\partial t^*} = \underbrace{\frac{3C_D|\boldsymbol{u}_S^*|}{4d_p^*\rho_P^*}\boldsymbol{u}_S^*}_{Drag} + \underbrace{\frac{3}{4}\frac{C_L}{\rho_P^*}(\boldsymbol{u}_S^* \times \boldsymbol{\omega}_F^*)}_{Lift} + \underbrace{\frac{1}{2\rho_P^*}\frac{D'\boldsymbol{u}_F^*}{Dt^*}}_{Virtual\ Mass} + \underbrace{\frac{1}{\rho_P^*}\frac{D\boldsymbol{u}_F^*}{Dt^*}}_{Pressure\ Gradient} \tag{5}$$

In Eqs. (4) and (5), $\boldsymbol{x_P^*}$ represents the coordinates of the particle position, $\boldsymbol{u_P^*}$ is the particle velocity, $\boldsymbol{u_S^*} = \boldsymbol{u_F^*} - \boldsymbol{u_P^*}$ is the particle-fluid slip velocity, d_P^* is the diameter of the particle non-dimensionalised by the channel half-height, ρ_P^* is the particle-fluid density ratio and $\boldsymbol{\omega_F^*}$ is the fluid vorticity at the particle position given by $\boldsymbol{\omega_F^*} = \boldsymbol{\nabla} \times \boldsymbol{u_F^*}$. The drag coefficient, C_D, is taken from standard empirical observations [17] and the lift term uses the Saffman-Mei [18, 19] coefficient. A fourth-order accuracy Runge-Kutta method was used to integrate Eqs. (4) and (5) to obtain each particle's new position and velocity at each fluid step. The timestep used in the integration scheme was equal to that of the fluid, $\Delta t_P^* = 0.01$.

2.3 Two-way coupling

To account for each particle's inertial feedback effect on the fluid phase, an additional source term in the Navier-Stokes equations was included:

$$\boldsymbol{f}_{2W,i}^* = \frac{1}{V_i^*}\sum_{j=1}^{N_P}\frac{\partial \boldsymbol{u}_{P,j}^*}{\partial t^*}, \tag{6}$$

where V_i^* is the volume of computational cell i, and N_P is the total number of particles in that cell. This is applied at each fluid flow timestep and uses the particle acceleration calculation from the previous timestep.

2.4 Four-way coupling

The LPT also considers hard-sphere inelastic collisions between binary particles in order to predict more accurately systems at increased volume fraction. It is assumed here that the time it takes for a full collision to occur (touch, contraction, expansion and recoil) is lower than the particle integration timestep. We also assume that any other interactions between the particles are negligible, other than in the case of van der Waals attraction (which is modelled separately). A deterministic binary search algorithm is also implemented as described in Breuer and Almohammed [20] in order to reduce the computational cost associated with collision identification from $O(N_P^2)$ to $O(N_P)$.

Once identified, resultant velocities and positions are determined using kinetic-energy and momentum conservation equations, with particles also deflected a short distance, accounting for the time they spent travelling 'inside' their collision partner.

2.5 Deterministic energy-based agglomeration model

Upon collision, particles satisfying a certain energetic condition will agglomerate with their partner, producing a larger particle with volume equivalent to that of the two initial particles. The model, which is based upon the work of Njobuenwu and Fairweather [13], assumes that a collision will produce an agglomeration event if the resulting collision energy (after dissipation due to inelastic collision) is insufficient to overcome the attractive van der Waals potential between the two colliders, accounting for plastic deformation at the contact surface. The requirement is:

$$\boldsymbol{u}^{*2}_{P,r} - \frac{(1-e_n^*)\left(\boldsymbol{u}^*_{P,r}\cdot\hat{\boldsymbol{n}}\right)^2}{\left|\left(\boldsymbol{u}^*_{P,r}\cdot\hat{\boldsymbol{n}}\right)\right|} \leq \frac{H^*}{6\delta_0^{*2}}\left[\frac{6(1-e_n^*)}{\pi^2\rho_P^*\bar{\sigma}^*}\left(\frac{d_{P,1}^{*3}+d_{P,2}^{*3}}{d_{P,1}^{*2}d_{P,2}^{*2}\left(d_{P,1}^{*2}+d_{P,2}^{*2}\right)}\right)\right]^{\frac{1}{2}}, \quad (7)$$

where $\boldsymbol{u}^*_{P,r}$ is the relative particle collision velocity, e_n^* is the coefficient of normal restitution, $\hat{\boldsymbol{n}}$ is a unit vector pointing from particle 2 to particle 1, H^* is the non-dimensional Hamaker constant of the fluid-particle phase, δ_0^* is the minimum contact distance, $\bar{\sigma}^*$ is the maximum contact pressure and $d^*_{P,i}$ is the diameter of particle *i*. If the requirement in Eq. (7) is met, then the particles agglomerate forming a new volume-equivalent spherical particle. The new diameter is therefore:

$$d^*_{agg} = \sqrt[3]{{d^*_{P,1}}^3 + {d^*_{P,2}}^3}. \quad (8)$$

Positions and velocities of the agglomerate are also adjusted accordingly. Specifically:

$$\boldsymbol{u}^*_{agg} = \frac{1}{{d^*_{agg}}^3}\left({d^*_{P,1}}^3\boldsymbol{u}^*_{P,1} + {d^*_{P,2}}^3\boldsymbol{u}^*_{P,2}\right), \quad (9)$$

$$\boldsymbol{x}^*_{agg} = \frac{1}{2}\left(\boldsymbol{x}^*_1 + \boldsymbol{x}^*_2\right), \quad (10)$$

where $\boldsymbol{u}^*_{agg}$ is the new velocity of the agglomerate and $\boldsymbol{r}^*_{agg}$ is the new position of the agglomerate.

3 RESULTS AND DISCUSSION

3.1 Unladen fluid flow statistics

The simulations were first performed unladen, allowed to develop from an arbitrary initial flow field to a state of statistically stationary turbulence. When the first and second moments of the velocity distribution across the channel were unchanging, the statistics were zeroed and new distributions were obtained between $0 \leq t^* \leq 300$, with t^* representing the time after the statistics were reset.

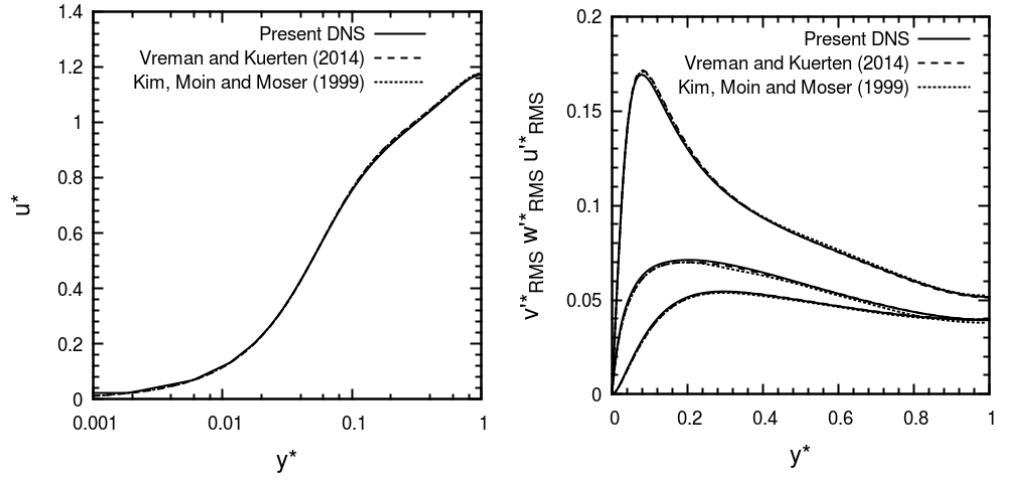

Figure 2: Statistical moments of unladen $Re_\tau = 180$ turbulent channel flow velocity field. Left: Mean streamwise velocity; Right: root mean square of streamwise, spanwise and wall-normal (top to bottom) velocity fluctuations. Present work (solid line) is compared with Vreman and Kuerten [21] (dashed) and Kim, Moin and Moser [22] (dotted).

The continuous phase predictions for mean streamwise velocity and turbulence intensities are presented in Fig. 2, which are compared to the work of [21] and [22] with excellent agreement obtained in all statistical moments considered.

3.2 Particle-laden flow statistics

Particles with diameters ranging between 202.5μm and 405.0μm were injected into the turbulent channel flow randomly throughout the domain. Initial velocities were set to be equivalent to that of the local fluid, obtained via spectral interpolation. The mechanical and chemical properties of each particle set are presented in Table 1.

Table 1: Particle-phase mechanical and chemical properties with dimensional equivalents based on calcite particles in a δ=0.02m water channel at $Re_\tau = 180$.

Parameter	St^+=0.5	St^+=1	St^+=2	Unit
St^+	0.5	1	2	-
St^*	0.043	0.086	0.173	-
τ_P	6.17	12.35	2.47	ms
ρ_P	2710	2710	2710	kg m^{-3}
ρ_P^*	2.71	2.71	2.71	-
d_P	202.5	286.4	405.0	μm
d_P^*	0.0101	0.0143	0.0202	-
d_P^+	1.82	2.58	3.64	-
Θ_P	10^{-3}	10^{-3}	10^{-3}	-
N_P	309,185	109,313	38468	-
Δt^*	0.01	0.01	0.01	-
Δt^+	0.12	0.12	0.12	-
A	3.8×10^{-20}	3.8×10^{-20}	3.8×10^{-20}	J
A^*	2.42×10^{-16}	2.42×10^{-16}	2.42×10^{-16}	-
δ_0	2.0×10^{-10}	2.0×10^{-10}	2.0×10^{-10}	m
δ_0^*	1.0×10^{-8}	1.0×10^{-8}	1.0×10^{-8}	-
$\bar{\sigma}$	3.0×10^{8}	3.0×10^{8}	3.0×10^{8}	Pa
$\bar{\sigma}^*$	0.15×10^{8}	0.15×10^{8}	0.15×10^{8}	-
e_N	0.4	0.4	0.4	-

All simulations presented here were performed four-way coupled with the post-collision agglomeration mechanism switched on. Figure 3 demonstrates the time evolution of the number of particle collisions and agglomerations over the course of the time period $0 \leq t^* \leq 50$, where t^* now refers to the time after particle injection. Note that all quantities here have been normalized by the initial number of particles, N_P, which differs in each simulation to preserve a constant volume fraction between the studies.

The left plot indicates a very similar collision rate for all three particle diameters, with the larger particles exhibiting fewer collisions. This is explicable by the constant volume fraction for all three sizes. Furthermore, the particle's possess similar Stokes numbers which are all in the tracer regime, and so particle-fluid interaction dynamics such as low-speed streak clustering will be minimal. The righthand plot indicates varied behaviour in terms of the number of agglomeration events over time. The rate is approximately constant for all three particle diameters, and is much greater for the smaller particles than for the larger ones. Particle size plays an important role in the energetics associated with Eq. (7), and so provided the particles collide, those with lower diameter are more likely to agglomerate. Clearly, as the particles in the system begin to agglomerate, the mean particle diameter will increase, meaning the agglomeration rate will start to decrease over time, since adhesion of large particles is unfavourable.

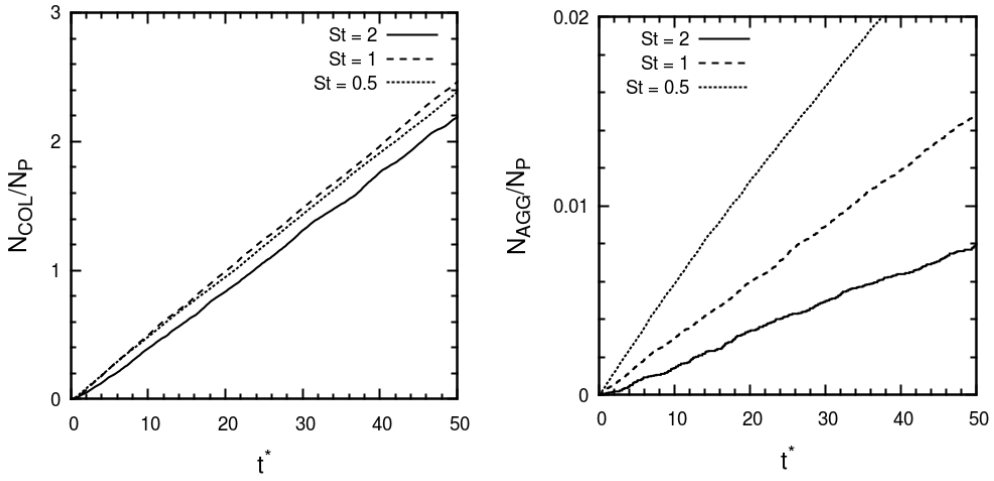

Figure 3: Effect of Stokes number on the temporal evolution of total number of particle-particle collision (left) and agglomeration (right) events normalized by the initial number of injected primary particles.

The left plot in Fig. 4 illustrates the rate of agglomeration, given a collision has occurred. After a short initial transient period, the rate reaches a steady state, with larger particles once again exhibiting lower frequency of agglomeration. Since this quantity is normalized by the number of collisions, it is expected that this rate will settle to a constant value as the simulation evolves. The right plot in Fig. 4 shows the evolution of the mean number of agglomerated primary particles over time. Again, we observe that the smaller particles exhibit more agglomeration events and as such, more primary particles form constituents of agglomerates as the simulation evolves.

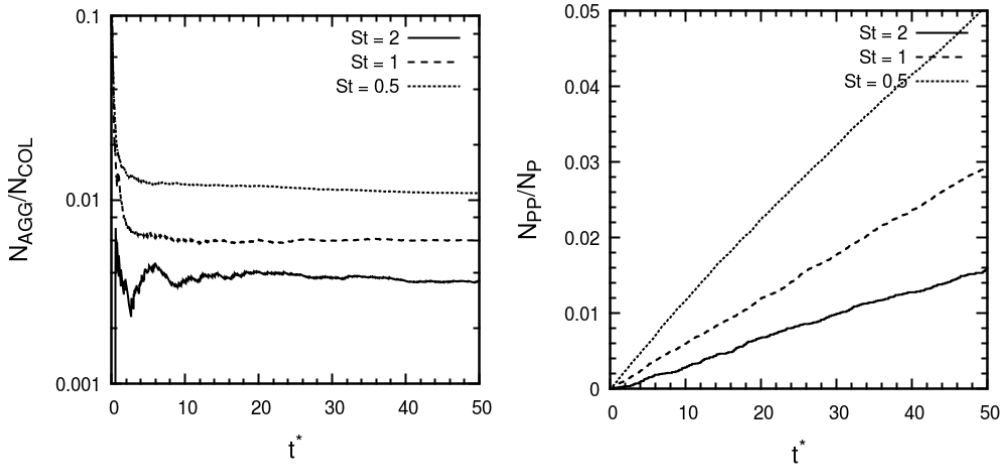

Figure 4: Effect of Stokes number on the temporal evolution of the agglomeration rate, N_{AGG}/N_{COL} (left) and on the mean number of agglomerated primary particles (right) normalized by the initial number of injected primary particles.

Figure 5 shows the time evolution of the percentage of agglomerates of size N, for each Stokes number particle type. As Stokes number increases, the rate at which N=2 and N=3 size agglomerates form is reduced. Over the timeframe studied, the number of N>2 size agglomerates formed is very low, accounting for below 0.1% of the total number of particles by the end of the simulation.

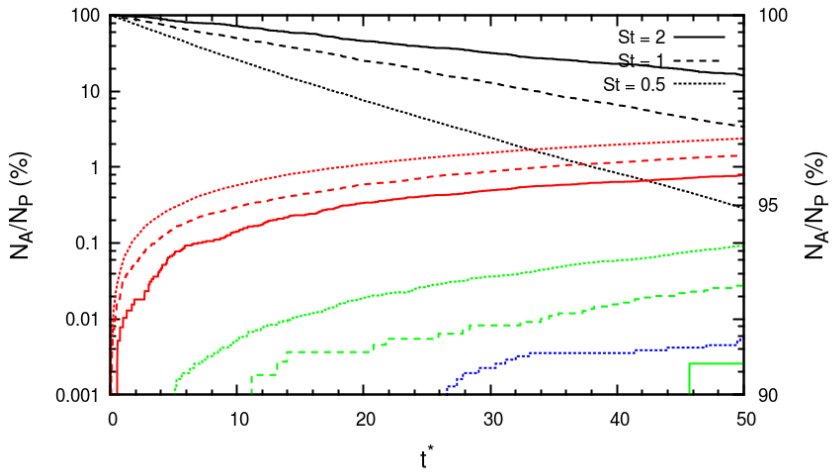

Figure 5: Effect of Stokes number on the temporal evolution of the number of agglomerates of size N. Black: N=1; red: N=2; green: N=3, blue: N=4.

To determine the variation in collision and agglomeration dynamics in the wall-normal direction of the channel flow, the collision and agglomeration rates have been sampled over the entire simulation time. These are plotted in Fig. 6, note that the scatter in the distributions is due to a limitation in the number of collision events which take place in the time sampled, but despite this the general trends are still evident. The left plot shows the number of collision events across the channel. The largest diameter particles show little variation in collision rate, whereas as the diameter is reduced, the particles at $St^+ = 1$ show more of a preference for collisions taking place in the wall region ($y^* < 0.2$). Although not plotted here, the same trend is observed for the wall-region local particle concentration around this Stokes number. This due to the strong preferential concentration exhibited by these particles, wherein the particle timescale and the fluid vortical timescales are similar. The right plot indicates the variation in agglomeration rate (given a collision has taken place) across the channel. Here, it is evident that the smallest particles actually show an increased agglomeration rate in the centre of the channel, despite the fewest collisions taking place within that region.

This last observation implies that the kinetics associated with agglomeration are more favourable closer to the channel centreline, which is to say that the collisions disperse more energy. Consulting Eq. (7), for a favourable agglomeration, either the term $\boldsymbol{u}^*_{P,r}$ must be small or the term $(1 - e^*_n)\left(\boldsymbol{u}^*_{P,r} \cdot \hat{\boldsymbol{n}}\right)^2 / \left|\left(\boldsymbol{u}^*_{P,r} \cdot \hat{\boldsymbol{n}}\right)\right|$ must be large within this region (or a combination of the two). Previous work [23] indicates an increase in collision angle close to the wall, hence the relative velocity will be large and the kinetic energy dispersed will be low leading to unfavourable conditions for agglomeration, despite the increase in particle concentration.

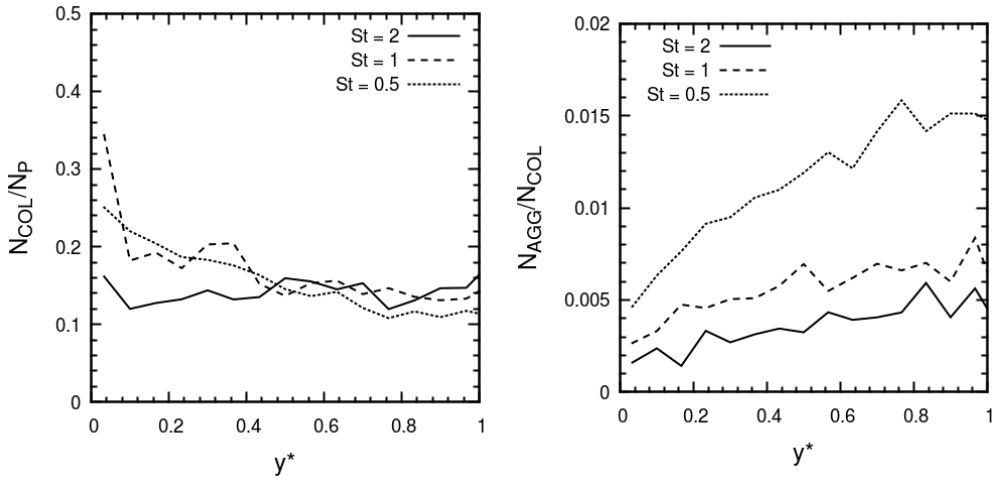

Figure 6: Effect of Stokes number on mean particle collision rate normalized by the initial number of injected primary particles (left) and mean particle agglomeration rate (right) across wall-normal direction of the channel. Sample time is $0 \leq t^* \leq 50$.

4 CONCLUSIONS

A deterministic energy-based agglomeration model has been applied to a DNS-LPT solver in order to determine the effect of particle diameter on collision and aggregation dynamics in multiphase turbulent channel flows. The continuous phase statistics have been validated against two very well regarded DNS databases at the same shear Reynolds number, with excellent agreement obtained.

Time evolution of various statistical quantities indicates that the system posseses a statistically steady state in terms of collision and agglomeration rate at $t^* > 10$, where t^* is the non-dimensional time after the particles have been injected. This persist throughout the entire simulation time considered here ($t^* \leq 50$). All three particle sizes considered exhibit similar collision rates when non-dimensionalized by the total number of injected primary particles, but agglomeration events are much enhanced for smaller particles. This is partially due to the inverse dependance of the required change in van der Waals attraction energy on particle diameter. Agglomeration rates (given a collision has occurred) are also observed to scale inversely with particle size, along with the mean number of primary particles which form a typical agglomerate in the system. Finally, collision and agglomeration rates across the wall-normal direction of the channel indicate that collisions favour the near-wall region. However, agglomeration events are actually more likely towards the channel centreline. We conclude that the bulk flow region posseses particles with favourable dynamic properties for agglomeration, whereas the wall region does not. It is likely that agglomerates forming in the centre of the channel at long timeframes may drift towards the walls through turbophoresis as their Stokes number increases, but these simulations should be extended to confirm such predictions.

5 ACKNOWLEDGEMENTS

This work was supported by a UK Engineering and Physical Sciences Research Council grant at the University of Leeds from the EPSRC Centre for Doctoral Training in Nuclear Fission – Next Generation Nuclear.

REFERENCES

[1] Folini, D., Ubl, S. and Kaufmann, P., Lagrangian particle dispersion modeling for the high Alpine site Jungfraujoch. *Journal of Geophysical Research: Atmospheres* (2008) **113**(18).

[2] Chen, R., Zhang, L., Zang, D. and Shen, W., Blood drop patterns: Formation and applications. *Advances in Colloid and Interface Science* (2016) **231**: 1-14.

[3] Guha, D., Ramachandran, P. and Dudukovic, M., Flow field of suspended solids in a stirred tank reactor by Lagrangian tracking. *Chemical Engineering Science* (2007) **62**(22): 6143-6154.

[4] Chun, J., Oh, T., Luna, M. and Schweiger, M., Effect of particle size distribution on slurry rheology: Nuclear waste simulant slurries. *Colloids and Surfaces A: Physicochemical and Engineering Aspects* (2011) **384**(1-3): 304-310.

[5] Krozel, J.W., Electrokinetic interactions between two spheres: The role of surface charge transport in coagulation. *Journal of Colloid and Interface Science* (1994) **163**(2): 437-453.

[6] Kuerten, J. and Vreman, A., Can turbophoresis be predicted by large-eddy simulation? *Physics of Fluids* (2005) **17**(1): 011701-011704.

[7] Wang, J., Shi, Q., Huang, Z., Gu, Y., Musango, L. and Yang, Y., Experimental investigation of particle size effect on agglomeration behaviors in gas–solid fluidized beds. *Industrial & Engineering Chemistry Research* (2015) **54**(48): 12177-12186.

[8] Henry, C., Mineri, J.P., Pozorski, J. and Lefèvre, G., A new stochastic approach for the simulation of agglomeration between colloidal particles. *Langmuir* (2013) **29**(45): 13694-13707.

[9] Schutte, K.C.J., Portela, L.M. and Twerda, A., Hydrodynamic perspective on asphaltene agglomeration and deposition. *Energy & Fuels* (2015) **29**(5): 2754-2767.

[10] Balakin, B., Hoffmann, A.C. and Kosinski, P., The collision efficiency in a shear flow. *Chemical Engineering Science* (2012) **68**(1): 305-312.

[11] Kosinski, P. and Hoffmann, A.C., Extended hard-sphere model and collisions of cohesive particles. *Physical Review E* (2011) **84**(3): 031303.

[12] Alletto, M., Numerical investigation of the influence of particle-particle and particle--wall collisions in turbulent wall-bounded flows at high mass loadings. (2014). PhD Thesis, Univ. der Bundeswehr, Hamburg (Germany).

[13] Njobuenwu, D.O. and Fairweather, M., Simulation of deterministic energy-balance particle agglomeration in turbulent liquid-solid flows. *Physics of Fluids* (2017) **29**(8): 083301.

[14] Vdović, N. and Bišćan, J., Electrokinetics of natural and synthetic calcite suspensions. *Colloids and Surfaces A: Physicochemical and Engineering Aspects* (1998) **137**(1-3): 7-14.

[15] Maxey, M.R. and Riley, J.J., Equation of motion for a small rigid sphere in a nonuniform flow. *Physics of Fluids* (1983) **26**(4): 883-889.

[16] Daitche, A., On the role of the history force for inertial particles in turbulence. *Journal of Fluid Mechanics* (2015) **782**: 567-593.

[17] Schiller, L. and Naumann, A., Fundamental calculations in gravitational processing. *Zeitschrift Des Vereines Deutscher Ingenieure* (1933) **77**: 318-320.

[18] Saffman, P., The lift on a small sphere in a slow shear flow. *Journal of Fluid Mechanics* (1965) **22**(2): 385-400.
[19] Mei, R., An approximate expression for the shear lift force on a spherical particle at finite Reynolds number. *International Journal of Multiphase Flow* (1992) **18**(1): 145-147.
[20] Breuer, M. and Almohammed, N., Modeling and simulation of particle agglomeration in turbulent flows using a hard-sphere model with deterministic collision detection and enhanced structure models. *International Journal of Multiphase Flow* (2015) **73**: 171-206.
[21] Vreman, A.W. and Kuerten, J.G.M., Comparison of direct numerical simulation databases of turbulent channel flow at $Re_\tau = 180$. *Physics of Fluids* (2014) **26**(1).
[22] Kim, J., Moin, P., and Moser, R., Turbulence statistics in fully developed channel flow at low Reynolds number. *Journal of Fluid Mechanics* (1987) **177**: 133-166.
[23] Rai, K., Mortimer, L.F. and Fairweather, M., Effect of Reynolds number on critical Stokes number in turbulent channel flow. in *ICMF2019* (2019) Rio de Janeiro, Brazil.